

*Original Research*

# Infiltration Characteristics of Surface Water in Coal Seam Mining Beneath Gullies and Corresponding Preventive Measures

Hongbo Shang<sup>1,2,3\*</sup>, Hao Wang<sup>2,3</sup>, Tiantian Wang<sup>2,3</sup>, Jiankun Xue<sup>2,3</sup>, Zhenfang Zhou<sup>2,3</sup>

<sup>1</sup>China Coal Research Institute, Beijing 100013, China

<sup>2</sup>Technology & Engineering, Xi'an Research Institute of China Coal (Group), Corp, Xi'an 710077, China

<sup>3</sup>Key Laboratory of Coal Mine Water Hazard Prevention and Control Technology in Shaanxi Province, Xi'an, Shaanxi, 710054, China

*Received: 6 February 2024*

*Accepted: 27 May 2024*

## Abstract

Surface water represents one of the crucial factors influencing the safety of shallow coal mining within the Western China mining region. The objective of this study was to investigate the infiltration properties of surface water in coal seam mining under gullies and to propose effective preventive measures. We selected the typical working face of the Buliangou coal mine as the study area and conducted a series of physical and mechanical tests on rock samples. Further, we employed the UDEC and COMSOL numerical models to examine the physical and mechanical properties, overburden mining fissures distribution laws, and surface water infiltration characteristics. We noted a good agreement between the measured (223.86 m) and modeled height (230-250 m) of the water-conductive fractured zone. When the working face advanced by 200 m, 250 m, and 300 m, the water-conductive fracture zone connected the surface, and the surface water in the gully infiltrated into the goaf along the fissure, resulting in a stable water volume of 41.9 m<sup>3</sup>/h, 56.9 m<sup>3</sup>/h, and 75.0 m<sup>3</sup>/h, respectively. In the former scenario, when the working face advanced by 200 m, 250 m, and 300 m, an excellent agreement was observed between the numerically derived (41.9 m<sup>3</sup>/h, 56.9 m<sup>3</sup>/h, 75.0 m<sup>3</sup>/h) and field measured (40.0 m<sup>3</sup>/h, 53.6 m<sup>3</sup>/h, 70.8 m<sup>3</sup>/h) stable water volume in the goaf. Consequently, the numerical model accurately predicted the water volume in the goaf from the surface water of the coal seam mining under the gully and can be utilized for further predictions under different advancing distances. Ultimately, we propose preventive measures to curtail the surface water infiltration, effectively barring the influx of surface water into the goaf, precluding the occurrence of a mine water disaster, and ensuring secure mining operations. The research results can provide theoretical guidance for the efficient prevention and control of surface water beneath gullies during the coal seam mining process.

**Keywords:** mining under gully, water-conductive fracture zone, numerical model, infiltration of surface water, stable water volume

---

\*e-mail: shanghb@foxmail.com;

Tel.: 18-729-598-695.

## Introduction

Coal serves as the primary energy source in China, fulfilling approximately 60 to 70 percent of the nation's energy requirements in 2018 [1, 2]. Coal usage is projected to reach 50 percent of China's total energy resources as early as 2030 [3].

The complex hydrogeological conditions of China's mines have long been associated with significant casualties and economic losses for a long time [4–8]. Currently, four major types of water disasters are observed in China, including high-pressure karst water inrush from the coal seam floor, water inrush in sandstone and the loose layer of coal seam roof, water inrush from abandoned small coal mines and old mine goaf, and water disasters caused by surface water infiltration [9–11]. A comprehensive investigation of these water disasters has been conducted in several studies, encompassing mine water inrush mechanisms [12–17], the risk prediction and evaluation of coal mine water disasters [18–21], and mine-water disaster prevention and control technologies [22–24].

Until now, the majority of research has been centered on the first three water disasters. However, literature is scarce regarding the infiltration characteristics of surface water in coal seam mining beneath gullies [6]. The western region of China serves as the primary source of coal, with Inner Mongolia alone producing over 1 billion tons of raw coal in 2019. [25, 26]. The coalfields in this region are characterized by shallow coal seam occurrences, diverse and fluctuating topography, and relatively well-developed loess gullies [12, 27]. During the coal seam mining process, the water-conductive fracture zone reaches the surface in the shallow buried and gully areas, resulting in significant surface damage [28–31]. Surface water is then transported into the goaf along the water-conductive fracture zone,

posing a grave threat to the safety of coal mines [32, 33]. Furthermore, the depletion of surface water and groundwater flow has a detrimental impact on the fragile ecological environment of the mines in Western China [34, 35]. Therefore, to facilitate the concurrent development of safe and efficient coal mining practices and ecological conservation in mining areas, it is crucial to investigate the infiltration characteristics of surface water in the coal seam mining beneath gullies.

The present study emphasizes on the typical working face of the Buliangou coal mine in the Zhungeer coalfield of Inner Mongolia intensively examining the infiltration characteristics of surface water in coal seam mining beneath gullies. Moreover, we suggest preventive strategies to curtail surface water infiltration. The outcomes of our research furnish guidelines for the safe and efficient operation of the working face, in line with the standards of Nature Journal.

## Study Area

The study area is located in the Zhungeer coalfield in China, which belongs to the Ordos Basin. The surface of the study area is covered by loess and aeolian sand, and the bedrock is exposed only in large gully areas. The terrain of this study area is highly complex, with well-developed branched gullies. Some of the important branched gullies within the range of the coalfield are Dabuliangou, Xiaobuliangou, Xizigou, Fangtangou, Ejiagou, and Qingshuigou. The branch gullies are specially developed, and flash floods occur in the rainy season, with a massive flow rate and strong hydrodynamic force that lead to severe soil erosion. During the mining of the No.6 coal seam in the coal mine, the water-conductive fracture zone develops to the surface in the shallow burial and gully area

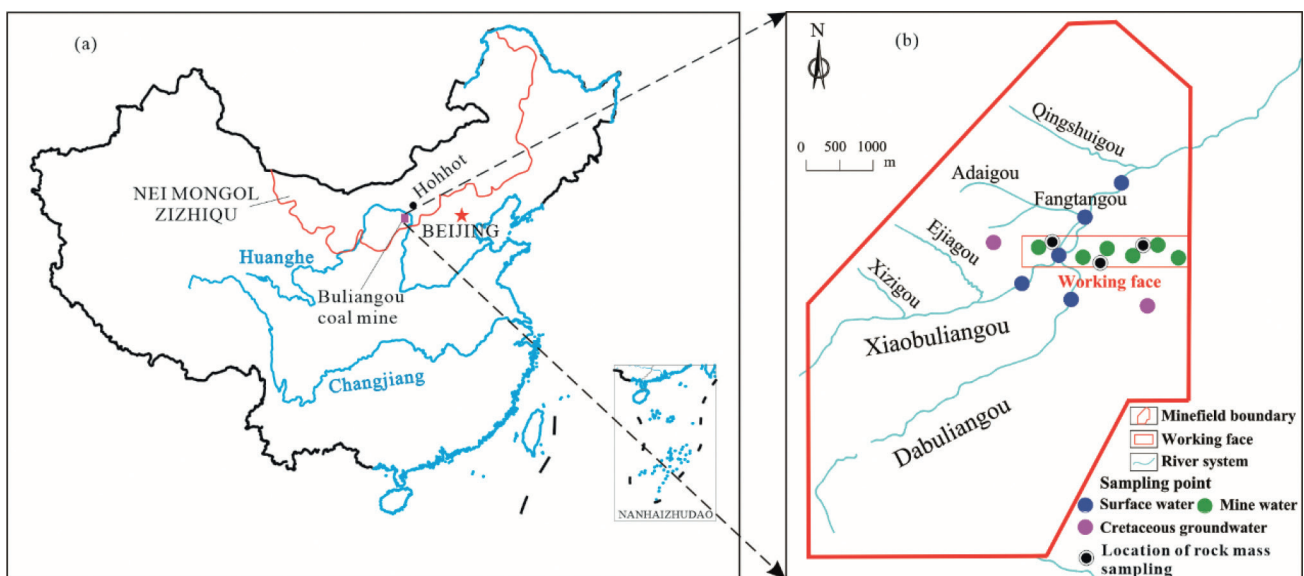


Fig. 1. Location of study area: a Buliangou coal mine in China, b Drainage map of well field and location of typical working face.

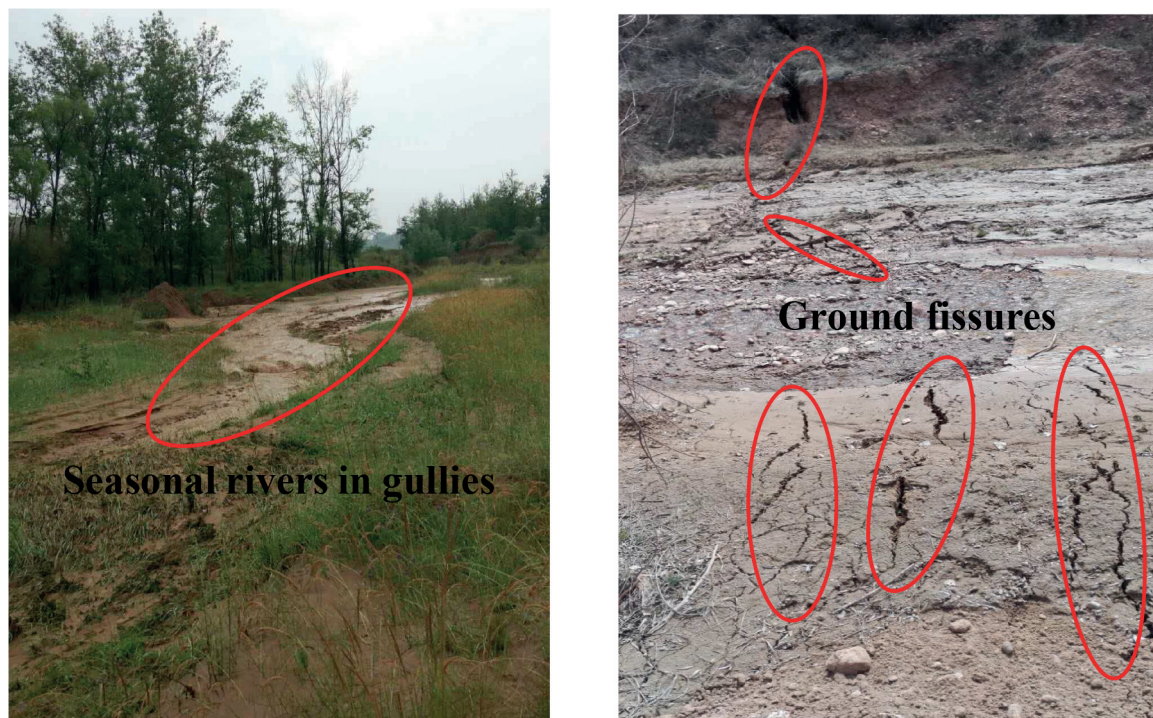


Fig. 2. Surface rivers and ground fissures.

within the coalfield, and the rainfall in the area is relatively concentrated. With the arrival of the rainy season, seasonal rivers form in the gully, and surface water enters the coal mine along the water-conductive fracture zone, giving rise to disastrous water inrush accidents. In the mining of the typical working face, seasonal rivers in surface gullies pass through this working face (Fig. 1). According to field observations, the water-conductive fracture zone had developed to the surface of the mine of this working face (Fig. 2). The surface river water will later enter the goaf along the fissure, causing water gushing in the coal mine and threatening the safety of production.

Therefore, it is imperative to investigate the infiltration characteristics and develop effective measures for preventing surface water ingress in typical working faces to ensure safe coal mining operations.

The general topography of the study area shows a high in the southwest and a low in the northeast, with an altitude of about +1110 ~ +1346 m. The average annual precipitation is 408 mm, while the maximum monthly rainfall is 247.5 mm. The total yearly evaporation in this region varies between 1824.7 and 2204.6 mm.

We selected the typical working face as our research object. In the coal mine, the 6<sup>th</sup> coal seam, which has a gentle inclination, is the main minable layer, with a thickness of 5.66–25.51 m. The buried depth varies between 166.80 and 478.00 m. According to the surface drilling exploration data, the strata in the minefield belonged to the periods (from old to new): Cambrian, Carboniferous, Permian, Cretaceous, and Quaternary. The comprehensive

pillar of the coal stratum in the typical working face is obtained from the average value of the thickness of each stratum in the data of 7 boreholes (Fig. 3).

The principal aquifers in the mining field include the Quaternary pore aquifer, the Cretaceous pore fissure aquifer, the Permian sandstone fissure aquifer, and the Ordovician karst fissure aquifer. Among them, the Quaternary pore aquifer, the Cretaceous pore fissure aquifer, and the Permian sandstone fissure aquifer are located above the 6<sup>th</sup> coal seam and have weak water abundance, and before the coal seam mining, the water bodies in the main aquifers of the roof have been drained in advance. During the mining process of the 6<sup>th</sup> coal seam, minimal infiltration from the roof aquifer was observed within the mine. In most sections of the mining field, there is a well-developed water-conductive fracture zone extending until the Quaternary system. Consequently, surface gully river water and atmospheric precipitation may pose significant hydrological risks to the 6<sup>th</sup> coal seam in this mining area.

## Materials and Methods

### Water Sampling and Analysis

Thirteen water samples were collected, with 5 representing surface water, 2 representing cretaceous groundwater, and 6 representing mine water. The sampling locations were recorded using a portable GPS device and visualized in Fig. 1. To ensure representative groundwater samples,

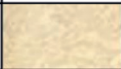
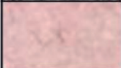
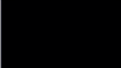
Comprehensive histogram of coal and rock strata in typical working face				
Stratigraphic unit	Columnar 1:500	Rock name	Thickness/ m	Lithology description
Quaternary Q		Loess layer	10.13	The surface is aeolian sand, alluvial proluvial sand gravel, mud, etc. Malan formation loess layer
Cretaceous K		Conglomerates with gravel	136.39	Fuchsia, the composition is mainly quartz feldspar, the composition of loose gravel is mainly granite gneiss, the diameter of the hard gravel is uneven, huge thick layer, with small pores in the middle
		Basalt	6.75	Dark gray, hard cemented tuffaceous, easy to be weathered in the upper and middle parts
		Conglomerates with gravel	19.26	Fuchsia, mainly quartz feldspar, the gravel composition is mainly granite gneiss
Permian P		Coarse-grained sandstone	8.32	Gray white, with quartz as the main part and a small amount of mica fragments
		Sandy mudstone	12.10	Gray dark gray, with a small amount of clay, sand structure, semi hard
		Fine-grained sandstone	7.26	Grey and white, followed by quartz feldspar, sand structure, massive structure
		Coarse-grained sandstone	15.06	Gray white, mainly quartz, followed by feldspar, uneven fractures and easy to break
		Sandy mudstone	18.48	Gray, muddy cement containing clay, semi-hard, transitional contact with underlying strata
		Coarse-grained sandstone	10.72	Gray yellow, mainly quartz feldspar, see mica flakes, semi-hard, well sorted
		Sandy mudstone	6.51	Gray, argillaceous cementation with a small amount of clayey soil
Carboniferous C		Coarse-grained sandstone	13.67	Yellow white, quartz feldspar, loose, strong water absorption, with cracks
		6 <sup>th</sup> Coal	15.60	Black, massive joint development, pyrite, high ash content, asphalt luster, dim-semi dim type coal, huge thick layer
		Fine-grained sandstone	1.62	Gray, mainly quartz feldspar
		Coarse-grained sandstone	46.13	Gray white, mainly quartz feldspar, locally containing gravel, gravel diameter is less than 0.02cm

Fig. 3. Typical working face stratum histogram.

groundwater was pumped for 5-10 minutes before collection to remove stagnant water. Sampled water was stored in white plastic bottles, which were rinsed 3–5 times using the water to be sampled. The bottles were then sealed, labeled, and transported to the laboratory for physicochemical analysis within 24 hours. All groundwater samples were analyzed for pH, total dissolved solids (TDS), and major ions ( $\text{Na}^+$ ,  $\text{K}^+$ ,  $\text{Ca}^{2+}$ ,  $\text{Mg}^{2+}$ ,  $\text{HCO}_3^-$ ,  $\text{SO}_4^{2-}$ ,  $\text{Cl}^-$ ). Prior to testing, all groundwater samples were filtered through 0.45  $\mu\text{m}$  membrane filters to remove suspended particulates in the laboratory. Major anions ( $\text{Cl}^-$ ,  $\text{SO}_4^{2-}$ ) were analyzed using an anion chromatograph with anion columns with detection accuracies of 1% (Thermo Company, Waltham, USA), while major cations ( $\text{Ca}^{2+}$ ,  $\text{Mg}^{2+}$ ,  $\text{Na}^+$ ,  $\text{K}^+$ )

were measured using a cation chromatograph with cation columns with detection accuracies of 1%. The accuracy of the analyses for all groundwater samples was verified by calculating the ionic balance error, with a 5% error limit considered the upper limit. Consequently, the calculated ionic balance errors for all groundwater samples were below the established limit.

#### Physical and Mechanical Property Tests of the Strata

Obtaining physical and mechanical parameters of the strata is the basis of the research to assess the distribution law of mining fissures in the overburden of coal seam mining. In order to elaborately understand the properties



Fig. 4. Rock samples.



Fig. 5. Experimental equipment diagram: a RTR-1500 rapid triaxial rock testing system, b Mercury porosimeter.

of each layer, the strata with different buried depths were sampled through the surface drilling of the typical working face (Fig. 4). Thereafter, the samples were transported to the laboratory for physical and mechanical tests, and the relevant experimental data was obtained. The rock samples from different strata were made into 50×100 mm standard samples. The RTR-1500 rapid triaxial rock testing system was used for the mechanical test, while the mercury porosimeter was used for the porosity test. The experimental equipment used in this study is shown in Fig. 5.

#### A Numerical Model of the Mining Fissures in Overburden in Gully Mining

Distribution characteristics of mining fissures in overburden in gully mining are the basis of studying surface

water infiltration [36]. The development characteristics of the mining fissures in the overburden after gully mining were analyzed using the UDEC software based on the engineering geological conditions and the drilling data of the typical working face in the study area [37]. In our study, we established a numerical model that conformed to the actual stratum. The length of the typical working face was 2118.3 m. The presence of a river crossing over the typical working face can be seen from the drainage map of the well field in Fig. 1. When the water-conductive fracture zone develops to the surface after coal mining, the seasonal river in the gully is expected to enter the mine along the fissure. The primary area where surface water enters the mine is in the vicinity of the seasonal river in the gully above the working face. Therefore, the area near the river in the gully was

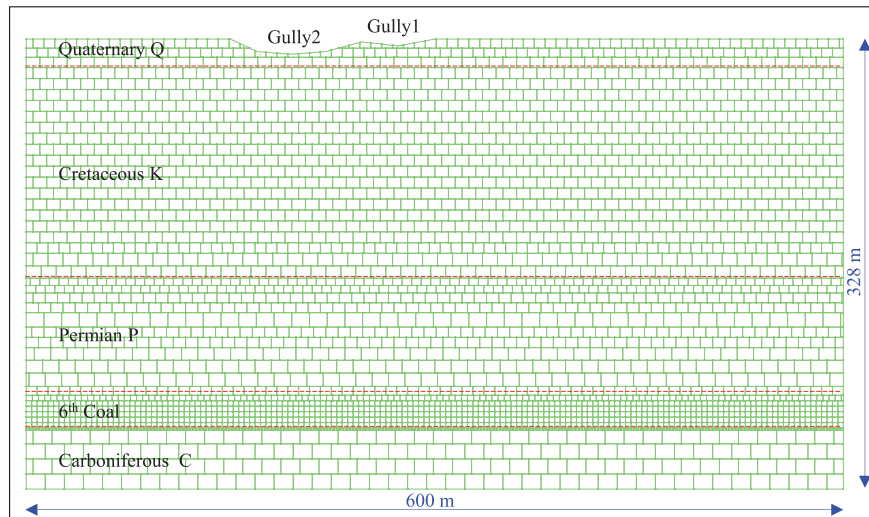


Fig. 6. Numerical model of overburden mining in gully mining.

Table 1. General chemistry of groundwater samples (mg/L).

number	sampling location	Water type	PH	K <sup>+</sup> +Na <sup>+</sup>	Ca <sup>2+</sup>	Mg <sup>2+</sup>	Cl <sup>-</sup>	SO <sub>4</sub> <sup>2-</sup>	HCO <sub>3</sub> <sup>-</sup>	TDS
1	Yellow River 1	Surface water	8.11	106.09	56.28	28.58	120.9	172.40	212.81	712.66
2	Yellow River 2	Surface water	8.1	106.36	56.47	28.37	121.57	173.13	211.12	711.07
3	Yellow River 3	Surface water	8.12	106.28	56.64	28.28	122.18	172.86	213.23	713.72
4	Yellow River 4	Surface water	8.81	8.86	35.68	56.28	11.8	20.00	296.67	457.66
5	Yellow River 5	Surface water	8.94	8.9	57.08	81.64	13.54	24.08	327.62	526.36
6	borehole 1	Cretaceous groundwater	9.1	324.32	31.08	31.73	407.61	59.30	145.17	936.62
7	borehole 1	Cretaceous groundwater	8.92	9.1	58.9	56.4	10.3	22.00	295.7	452.4
8	underground coal mine	Mine water	7.82	74.13	269.9	88.98	93.05	292.93	225.63	1045.42
9	underground coal mine	Mine water	7.32	37.38	146.1	83.88	50.71	87.11	263.78	670.39
10	underground coal mine	Mine water	8.27	41.86	192.4	61.09	150.33	75.42	674.43	1230.37
11	underground coal mine	Mine water	7.42	21.26	166.5	51.59	98.42	81.43	456.41	875.61
12	underground coal mine	Mine water	7.28	49.22	134.1	111.87	66.43	90.20	376.56	828.39
13	underground coal mine	Mine water	7.29	20.84	30.65	151.89	57.16	33.80	489.73	784.07

selected, and a two-dimensional numerical model with a length of 600 m and a height of 328 m was established according to a comprehensive histogram of the stratum. The thickness of the coal seam was 15.6 m. According to the actual gully position and depth above the working face, we set two gullies in the model; the gully 1 was about

6 m deep, and the gully 2 was about 10 m deep (Fig. 6). The left, right, and lower boundaries of the model were fixed by displacement. Confining pressure was applied to the left and right boundaries to simulate the actual stress of the slope. The parameters used in the numerical model were obtained by physical and mechanical tests (Table 1).

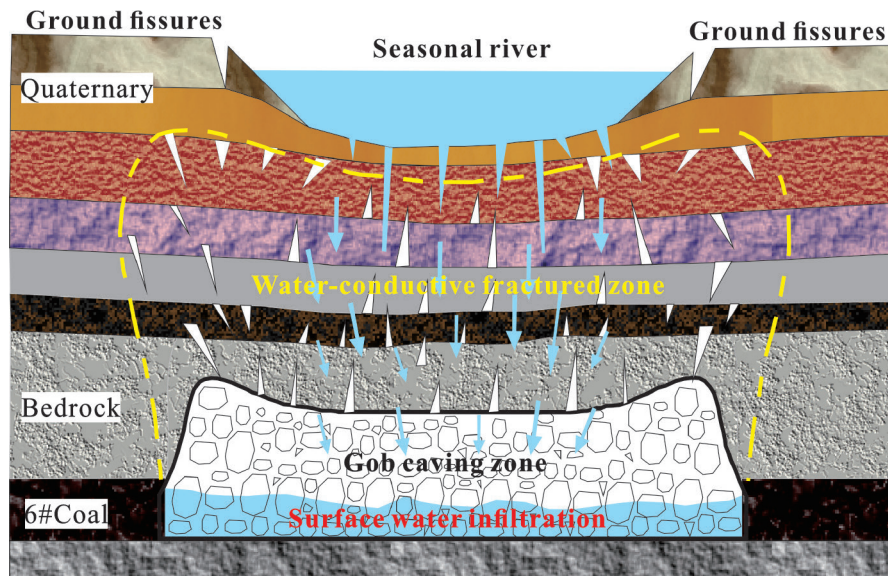


Fig. 7. Engineering geological model of surface water infiltration.

### A Numerical Model of Surface Water Infiltration

#### *Engineering Geological Model of Surface Water Infiltration*

Gully mining causes varying degrees of damage to the overburden, which then results in corresponding impacts on the surface water resources. After coal seam mining, the water-conductive fracture zone connects with the surface, leading to a leakage of the surface water. Thereafter, seasonal rivers formed in the gully enter the mine along the water-conductive fracture zone, threatening the safety of the mine [1, 12]. The engineering geological model of surface water infiltration is shown in Fig. 7.

#### *Construction of Surface Water Infiltration Model*

##### (1) Model construction and mesh generation

We aimed to investigate the infiltration characteristics of surface water through fissures following coal mining and quantify the volume of surface water infiltrating into the mine. Additionally, we aim to provide guidelines for preventing mine water disasters based on our findings. Considering the development characteristics of mining fissures in the overburden, we imported these fissures into COMSOL software to construct a numerical model simulating surface water infiltration after coal mining [38]. Herein, we present the numerical model and mesh generation using a scenario where the working face advances by 200 m as an example (Fig. 8).

##### (2) Calculation of model parameters and boundary conditions

The surface water mainly enters the mine along the fissure formed by mining. The surface water finds

it difficult to penetrate the regions of the mine where the rest of the mining fissures are not connected with the surface. Therefore, to simplify the model, the areas other than the mining fissures were regarded as a whole, and the parameters of the whole stratum were used to perform the corresponding numerical calculations. According to the field water injection test, the permeability coefficient of the Cretaceous, Permian, and Carboniferous aquifer was 0.0194 m/d, 0.021–0.081 m/d, and 0.0056–0.0577 m/d, respectively. The average of the permeability coefficient of the three aquifers (0.0340 m/d) was used as a representative of the permeability coefficient of the stratum. According to the conversion formula  $\kappa = \frac{k \rho g}{\mu}$  between permeability coefficient and permeability, the calculated permeability of the stratum was  $4.02 \times 10^{-14} \text{ m}^2$ . According to the average porosity of each stratum in Table 1, the porosity of the whole stratum was defined as 0.05.

Using the fracture flow module in COMSOL software, calculate the amount of surface water entering the goaf through mining fissures. The surface water flow in the mining fissures is in general much faster than in the surrounding porous matrix. The cubic law is a common correlation for modeling fissure flow. It defines the permeability  $k_f$  in the mining fissures according to

$$k_f = \frac{d_f^2}{12f_f} \tag{1}$$

where  $d_f$ (m) is the fissure's width and  $f_f$  is the roughness factor. The value of  $d_f$  can be obtained from the numerical model of the mining fissures in overburden in gully mining; The value of  $f_f$  in numerical calculations is 1. Finally, the permeability of the mining fissures in the numerical

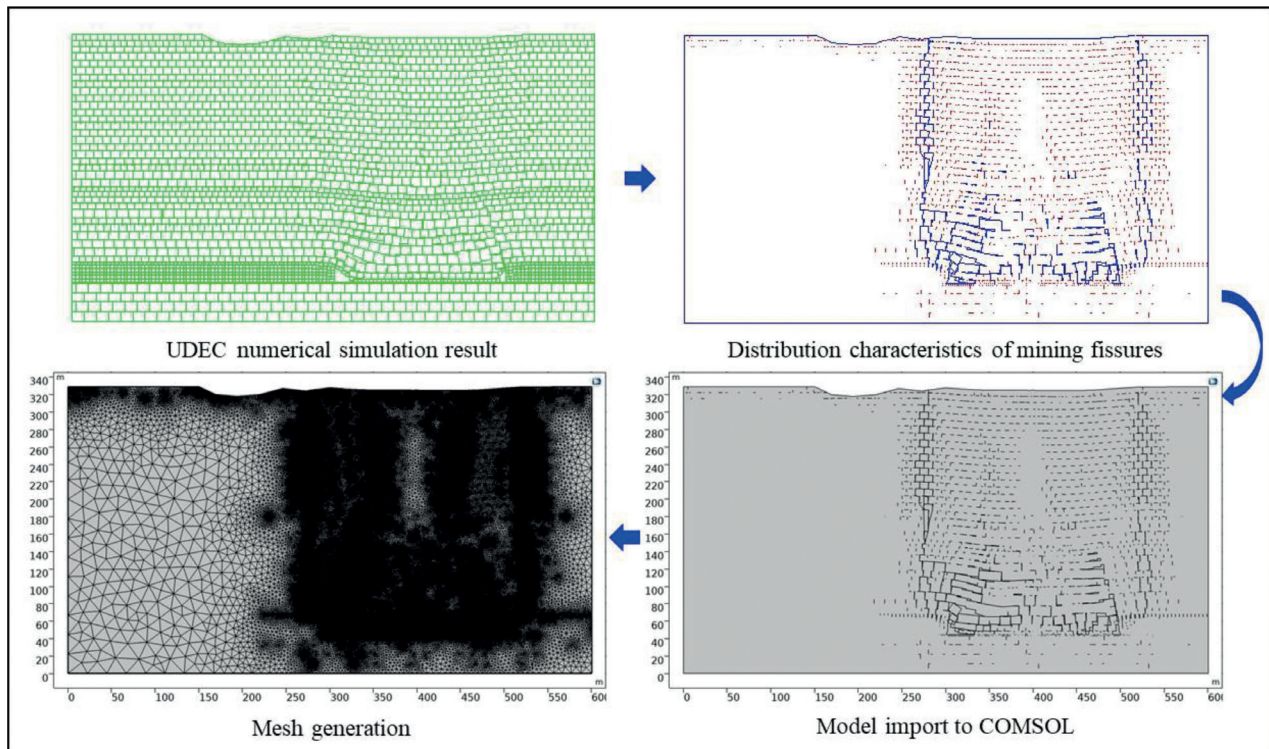


Fig. 8. Numerical model of surface water infiltration: a Model import, b Mesh generation.

model of surface water infiltration can be calculated using the above formula.

Two gullies were set at the upper boundary of the model. With the arrival of the rainy season, seasonal rivers will form in the gullies. The water level in the gullies during the rainy season reaches a height of about 1 m. Therefore, according to the actual situation, the boundary of the model gully was set as 1 m water head. The left, right, and bottom boundaries of the model were selected as the no-flow boundaries. The goaf boundary was designated as the free flow boundary. The surface water in the gully entered the goaf along the fissure.

## Results and Discussion

### Water Hydrochemistry

To delve into the general hydrochemistry of groundwater, the physicochemical parameters of the samples from surface water, cretaceous groundwater, and mine water are presented in Table 1.

The pH values of water samples within the study area exhibit a range of 7.32 to 9.1, indicating the presence of weakly alkaline water. The average pH values for surface water, chalk aquifer groundwater, and mine water are 8.42, 9.01, and 7.57, respectively. The TDS values of the various water samples range from 457.66 to 1230.37,

with some samples exhibiting highly mineralized waters. The average TDS values for surface water, chalk aquifer groundwater, and mine water are 624.29, 452.4, and 905.71, respectively. The pH value and TDS of mine water exhibit a closer resemblance to surface water compared to other samples. The main anions in surface water consist of  $\text{HCO}_3^-$  and  $\text{SO}_4^{2-}$ , while the primary cations are  $\text{SO}_4^{2-}$ . The order of major ions concentration in surface water samples is  $\text{HCO}_3^- > \text{SO}_4^{2-} > \text{K}^+ + \text{Na}^+ > \text{Ca}^{2+}$ . The main anions in Cretaceous groundwater are  $\text{HCO}_3^-$  and  $\text{Cl}^-$ , while the primary cations are  $\text{Na}^+$  and  $\text{K}^+$ . The main anions in mine water are  $\text{HCO}_3^-$  and  $\text{SO}_4^{2-}$ , with the primary cations being  $\text{SO}_4^{2-}$ . Clearly, the main ion composition of mine water exhibits a greater similarity to surface water compared to other samples.

The Piper (1944) trilinear diagram is very helpful in determining connections between different dissolved constituents and types of groundwater based on their chemical characteristics. Based on Table 1, the Piper trilinear diagram was drawn (Fig. 9a). The main hydrochemical type of mine water is  $\text{HCO}_3\text{-Ca}$ , while the main hydrochemical types of surface water are  $\text{HCO}_3\text{-Ca}$  and  $\text{SO}_4^{2-}\text{-Ca}$ . The primary hydrochemical type of groundwater in the Cretaceous system is  $\text{SO}_4^{2-}\text{-Na}$ . The results of the hydrochemical analysis indicate that mine water mainly originates from surface water. The analysis of hydrochemical types indicates that the main source of mine water is surface water. The  $\delta\text{D}$  and  $\delta^{18}\text{O}$  values in water are generally less affected by

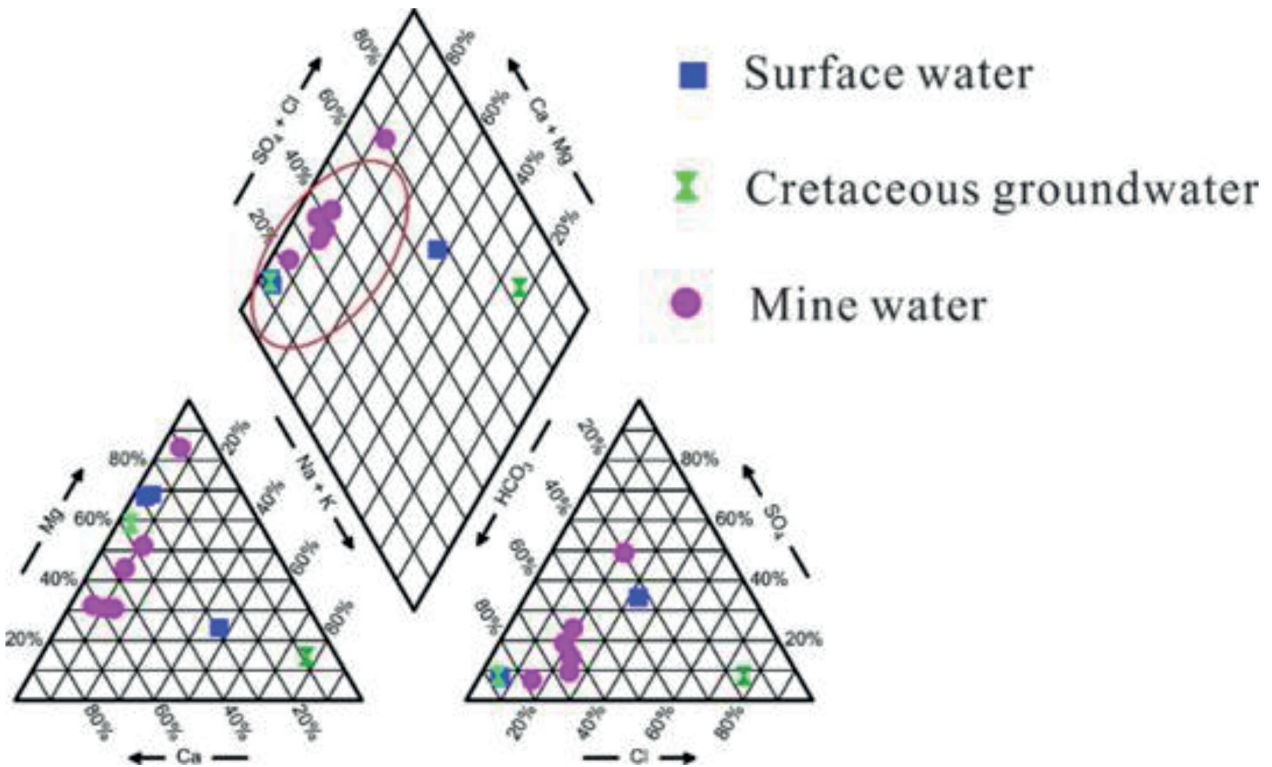


Fig. 9. Water Hydrochemistry of water samples.

water-rock interactions, making them effective means to determine different water sources and origins. A  $\delta D$ - $\delta^{18}O$  diagram (Fig. 9b) was constructed based on the  $\delta D$  and  $\delta^{18}O$  values of surface water, Cretaceous groundwater, and mine water. The atmospheric precipitation equation was calculated using the  $\delta D$  and  $\delta^{18}O$  values of atmospheric precipitation:  $\delta D = 9.38\delta^{18}O + 7.38$ . It is evident that the average values of surface water and cretaceous groundwater, as well as their respective  $\delta D$  and  $\delta^{18}O$  values, fall near the local atmospheric precipitation line, indicating that their main source of recharge is atmospheric precipitation. Furthermore, the proximity between surface water and mine water points demonstrates that mine water primarily originates from surface water.

#### Physical and Mechanical Properties of the Strata

The experimental data was arranged and summarized to get the physical and mechanical parameters of different rock samples, including compressive strength, tensile strength, modulus of elasticity, Poisson's ratio, cohesion, internal friction angle, porosity, and bulk density (Table 2). The physical and mechanical properties of the strata obtained from tests presented in Table 2 serve as crucial modeling parameters for establishing a more realistic numerical model of mining fissures in gully mining. Using the parameters in Table 2, we established a numerical model of the mining fissures in overburden in gully mining,

and the distribution characteristics of mining fissures obtained by the model were imported into COMSOL software to construct a numerical model simulating surface water infiltration after coal mining.

The rock mass strength and porosity data in Table 2 indicate that the rock mass above the roof of the 6th coal seam exhibits a layered structure characterized by soft and hard interphase. This type of layer structure, when subjected to mining disturbance, promotes extensive development of mining fissures in the overburden [39], as further confirmed by subsequent numerical simulations.

#### Numerical Simulation Results and Analysis of the Mining Fissures of Overburden in Gully Mining

Our model primarily analyzed the evolution process of the mining fissures in the overburden of the gully mining coal seam. The specific simulation scheme was set to advance from right to left. Considering the influence of the model boundary, the boundary coal pillars were reserved for 100 m, and each advancement was carried out in steps of 50 m, with a total advancement of 300 m. Distribution characteristics of mining fissures in the overburden of coal seam in gully mining have been shown in Fig. 10.

After coal mining, the roof strata moved and underwent deformation to produce open and closed fissures [40, 41]. In Fig. 10, the red part represents the closed fissures, while

Table 2. Formation physical and mechanical parameters.

Sampling horizon	Lithology	Thickness /m	Compressive strength /MPa	Tensile strength /MPa	Porosity /%	Modulus of elasticity/ 10 <sup>4</sup> MPa	Poisson's ratio	Cohesion / MPa	Internal friction angle/°	Bulk density /g/cm <sup>3</sup>
Quaternary	Loess layer	10.13	/	/	1.13	/	/	0.05	28.31	1.42
	Conglomerates with gravel	136.39	7.61	0.24	2.24	1.30	0.27	1.58	26.82	2.34
Cretaceous	Basalt	6.75	87.24	6.14	1.22	4.97	0.16	10.51	38.17	2.68
	Conglomerates with gravel	19.26	12.87	0.58	9.13	1.35	0.21	3.78	29.49	2.38
Permian	Coarse-grained sandstone	8.32	19.15	1.07	7.13	1.47	0.26	3.19	32.35	2.36
	Sandy mudstone	12.10	26.21	1.45	3.82	2.39	0.23	3.81	35.14	2.44
	Fine-grained sandstone	7.26	80.17	5.16	1.24	4.63	0.18	8.86	39.21	2.71
	Coarse-grained sandstone	15.06	36.52	2.07	3.19	2.08	0.22	5.13	33.42	2.38
	Sandy mudstone	18.48	27.36	1.20	3.03	1.12	0.25	4.57	32.63	2.43
Carboniferous	Coarse-grained sandstone	10.72	43.18	2.34	7.94	2.62	0.19	6.21	37.12	2.56
	Sandy mudstone	6.51	27.29	1.25	8.33	1.35	0.23	3.78	34.62	2.47
	Coarse-grained sandstone	13.67	61.28	3.51	13.60	3.56	0.17	7.21	36.76	2.36
Carboniferous	6 <sup>th</sup> Coal	15.60	20.65	0.78	8.64	0.16	0.28	2.47	24.37	1.42
	Fine-grained sandstone	1.62	34.66	1.71	4.09	1.83	0.21	4.98	35.85	2.52
	Coarse-grained sandstone	46.13	26.59	1.33	5.52	1.29	0.23	4.49	31.74	2.46

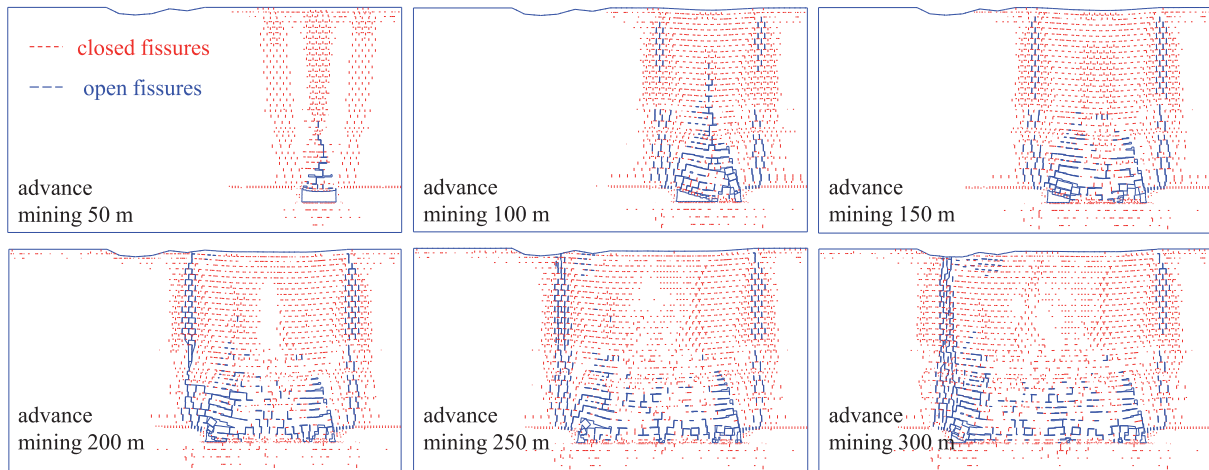


Fig.10. Development characteristics of mining fissures under different advance distance.

the blue part represents the open fissures, which comprise abscission and cross fissures. The penetration of the cross fissures into the layered rock and subsequent communication with the abscission layer produces a fluid migration channel or a water-conductive fracture zone [42]. Reference [43] employs PFC numerical simulation software to establish a numerical model of mining-induced fractures in the overlying rock of shallow seam mining through gully mining. It simulates the development characteristics and analyzes the evolution law of these fractures. In this study, we analyzed the development law of mining-induced fractures in the overlying rock during coal seam overlying mining. By comparing our results with those presented in reference [43], we observe consistency in both the simulated development characteristics of mining-induced fractures and the description and analysis of their development process in the overlying rock.

The distribution characteristics of mining fissures in the overburden under different advancing distances of the working face are depicted in Fig. 10. As the working face advanced to a distance of 50 m, abscission fissures emerged along with the upper part of the basic roof. Additionally, a few longitudinal fissures became evident in the middle section of the goaf. As the working face continued to advance, the immediate roof mudstone fell with the mining [44]. When the working face advanced to 100 m, the first collapse of the basic roof occurred; that is, the first pressure occurred. At this stage, the collapsed height was about 38 m away from the coal seam roof, and the height of the water-conductive fracture zone was 98 m. The increase in the advancing distance of the working face led to the periodic collapse of the old roof. Besides, the collapse height of overburden and the development height of the water-conductive fracture zone also changed. When the working face advanced to 200 m, the water-conductive fracture zone developed to surface

gully 1. Likewise, when the working face advanced to 300 m, the water-conductive fracture zone developed to surface gully 2. Under this scenario, the water-conductive fracture zone directly ran through the surface of the ground. Further, the compaction area was formed in the middle of the goaf due to the action of the mine pressure, and the density of the mining fissures in the compaction area was reduced. Since the stratum was composed of soft and hard structures, the development range of the mining fissure was extensive, and the mining fissure was mainly concentrated in the rock mass above the cut hole and the working face [45, 46]. After coal mining, the water-conductive fracture zone developed to the surface, and the seasonal river water in the gully entered the mine along the water-conductive fracture zone, resulting in disastrous water inrush accidents [47]. The numerically calculated maximum height of the water-conductive fracture zone ranged from 230 to 250 m. The development height of the water-guiding fracture zone is determined through the observation method of drilling flushing fluid leakage. This comprehensive approach involves direct measurements of drilling flushing fluid leakage, drilling water level, drilling speed, and observations of drilling anomalies (such as sticking, dropping, and air suction), as well as drilling coring observations and geological descriptions. Currently, it is considered the most reliable method for determining the extent of water-conducting fracture zone development in overlying strata. The final field test confirmed that the development height of the water-conducting fracture zone was 223.86m. These numerical results were found to be consistent with field measurements, indicating the reasonableness of the numerical model used for overburden failure in gully mining. This provides a solid foundation for subsequent numerical calculations related to surface water infiltration.

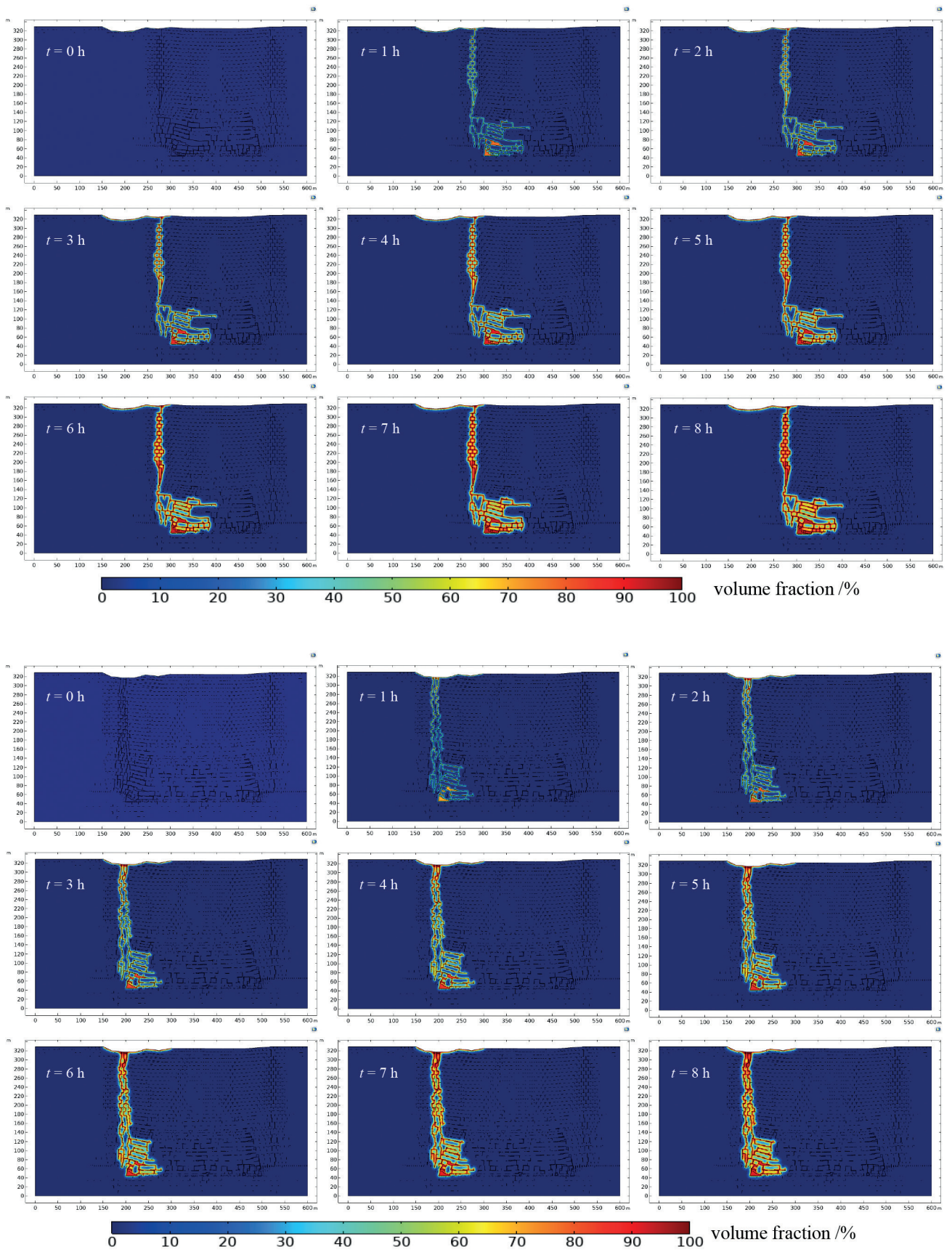


Fig. 11. Characteristics of surface water infiltration: a Advance mining 200 m, b Advance mining 300 m.

### Numerical Simulation Results and Analysis of Surface Water Infiltration

Based on the above model construction, mesh generation, and boundary conditions, the infiltration characteristics of surface water under different advancing distances of the working face are simulated and analyzed. Fig. 10 shows when the working face advanced by 50 m, the mining fissures did not communicate with the surface. When the working face advanced by 200 m, the mining fissures developed until the surface gully 1. When the working face advanced by 300 m, the mining fissures extended up to the surface gully 2. Therefore, in order to investigate the infiltration characteristics of surface water influenced by mining fissures, two working conditions (surface connected with a surface advancing distance of 200 m and 300 m) were selected for further numerical calculations to determine the volume of surface water. (Fig. 11).

Saturation was used to characterize the infiltration characteristics of surface water in the numerical calculation results. In Fig. 11, the red part represents the saturation of the surface water is 1 in the mining fissure, indicating that the surface water is full of mining fissures. The blue section shows null saturation of the surface water, that is, no surface water enters the mine. Fig. 11 illustrates that when the working face advanced 200 m, the mining fissures connected with the surface, and the fracture zone developed up to the surface gully 2. After one hour, the surface water in gully 2 began to infiltrate the goaf and converged there along the fissure, resulting in a significantly higher saturation of surface water in the goaf and the large mining fissures above it than in other mining fissures. As time progresses, the volume of surface water in mining fissures and goaf gradually increases, accompanied by an increase in saturation. When the working face advances 300 m,

the development of mining fissures becomes relatively prominent, extending up to the surface gully 1. The surface water within the gully infiltrates into the goaf through these mining fissures and converges with larger fractures above. Over time, this leads to a gradual increase in the saturation of surface water within both the mining fissures and goaf until it reaches a stable level. This phenomenon occurs due to continuous seepage of surface water into the mining fissures, eventually filling them up and establishing a steady flow towards the goaf.

To further analyze the infiltration characteristics of surface water and quantify the amount of surface water entering the goaf, we performed a real-time integration of the velocity  $u$  in the goaf area, i.e.  $Q = \iint u d\Omega$  (integral to get the water volume  $Q$  of surface water infiltrating goaf). Only surface water entering through mining-induced fissures was considered while disregarding water from seam roof aquifers that enters through such fissures. This is due to the presence of underground drainage boreholes constructed before coal seams are mined in the research area, effectively pre-draining the main aquifer of working face roofs. Field observations indicate minimal post-mining inflow after coal seams have been extracted; however, when mining fractures intersect with surface rivers or streams in gullies, surface water can infiltrate along these fractures. We report the amount of water infiltrating the goaf under the five conditions with variable advancing distances of the working face (50 m, 100m, 150m, 200 m, 250m, and 300 m) (Fig. 12).

Fig. 12 shows when the working face advanced 50 m, 100 m, and 150 m, the mining fissures were not connected with the surface, and the surface water failed to enter the goaf. Under this scenario, the water volume in the goaf was expectedly 0 m<sup>3</sup>/h. When the working face advanced 200 m, the mining fissures communicated with the surface,

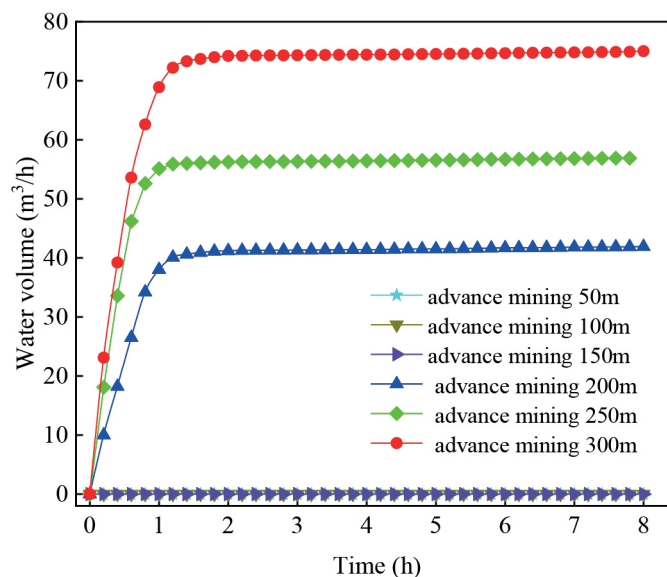


Fig. 12. Time varying curve of water quantity in goaf under different advancing distances.

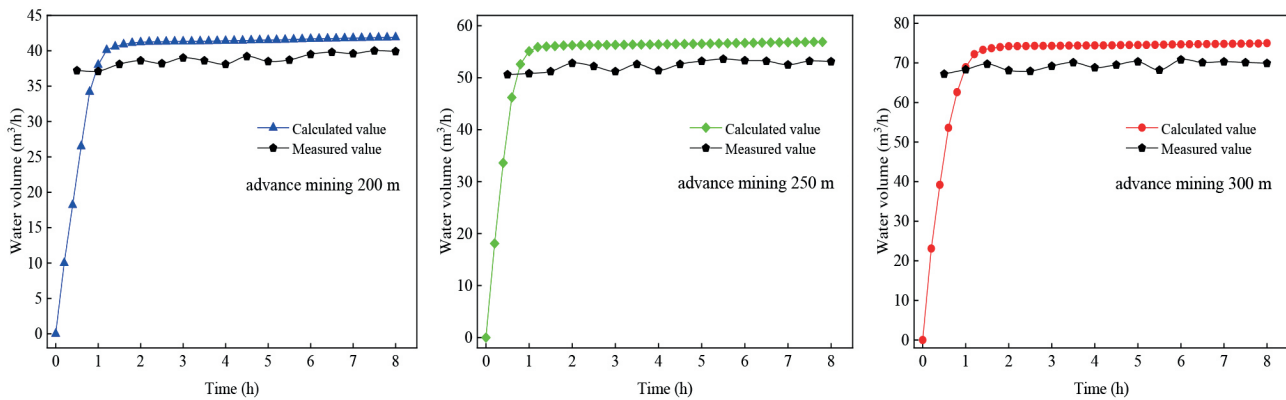


Fig. 13. Time varying curve of water quantity in goaf.

and the surface water infiltrated into the goaf along the fissures. The water volume increased to about  $41.9 \text{ m}^3/\text{hour}$  and then reached a stable state. When the working face advanced 250 m and 300 m, the water volume of surface water infiltrating the goaf rose to about  $56.9 \text{ m}^3/\text{hour}$  and  $75.0 \text{ m}^3/\text{hour}$  before reaching a steady state. The development of mining fissures was more thorough when the working face advanced 300 m, and many water diversion channels were formed.

To further validate the numerical calculations, we conducted an analysis of scenarios where the working face advanced by 200 m, 250 m, and 300 m. We compared and analyzed the field measurements with the temporal variation law of water volume in the goaf (Fig. 13).

Fig. 13 illustrates that with the increase of time, the water volume in the goaf calculated by numerical calculation increased rapidly at first and then gradually became stable. When the working face advanced 200 m, 250 m, and 300 m, the calculated water volume after the final stability was about  $41.9 \text{ m}^3/\text{hour}$ ,  $56.9 \text{ m}^3/\text{hour}$ , and  $75.0 \text{ m}^3/\text{hour}$ , respectively. The average measured stable water volume in the goaf was about  $40.0 \text{ m}^3/\text{hour}$ ,  $53.6 \text{ m}^3/\text{hour}$ , and  $70.8 \text{ m}^3/\text{hour}$ . The calculated water volume was slightly higher than the field-measured value, with errors of 4.53%, 5.80%, and 5.60%, respectively. These errors are within the allowable range of the project. Therefore, the magnitude of difference between the field measurement and the numerical calculation is small, which confirms the reliability of the latter.

We demonstrate that numerical calculation can provide an accurate estimate of the volume of surface water entering the goaf under different advancing distances. These results can then provide a scientific foundation for the mine water disaster prevention plan and underground drainage capacity design.

### Measures to Prevent Surface Water Infiltration

The continuous advancement of the typical working face leads to the gradual development of the mining fissures which

communicate with the surface. Once a large through type fissure is formed due to the scouring effect of the surface water, the water will flow into the mine in large quantities, resulting in a significant increase in the water volume of the goaf, causing mine water damage. Therefore, it is crucial to outline corresponding prevention measures for surface water infiltration and ensure the safety of mine production.

### Surface Fissure Backfilling

The development of mining-induced fissures in coal mining operations can lead to surface subsidence and the diversion of seasonal river water into the mine. Therefore, it is crucial to backfill these fissures that connect with the surface. For larger surface fissures, we recommend a two-step approach: initially backfilling a certain amount of gravel at the bottom, followed by compact clay backfilling in the upper portion. In gully areas, a compact and layered clay backfilling method should be employed first. Subsequently, sealing off any leakage points with clay, gravel, and cement will create an impermeable artificial riverbed to prevent the infiltration of surface water during rainy seasons.

### Construction of Soil and Water Conservation Forest

A protective forest should be built on both sides of the gully above the working face, as per the local climatic conditions to ensure soil and water conservation. Rigid and drought-resistant trees should be selected to effectively regulate the surface runoff and reduce the soil erosion caused by seasonal rivers in the gully. This will help in achieving soil stabilization and slope stabilization.

### Reasonable Arrangement of Mining Times

There are several seasonal surface runoff gullies in the mining area during the monsoon season. Therefore, the majority of mining should be carried out in the dry season to avoid the flood in the rainy season. This can

effectively prevent surface water from entering the mine. However, the specific prevention and control measures must be matched with the mining planning of the mine.

### Conclusion

(1) With the progression of the typical working face, the water-conductive fracture zone continuously evolved. Upon the advancement of the working face by 200 meters, the water-conductive fracture zone extended to the surface. In the numerical calculations, the maximum height of the water-conductive fracture zone was estimated to be 230-250 meters, while the measured value was 223.86 meters. Thus, the numerical calculations were consistent with the field measurement results.

(2) The infiltration model of surface water in coal seam mining was established using the COMSOL software based on numerical simulation outcomes. When the working face advanced by 50 m, 100 m, and 150 m, there were no connections between the mining fractures and the surface, resulting in negligible water volume in the goaf. However, as the working face advanced by 200 m, 250 m, and 300 m respectively, surface water infiltrated into the goaf through mining fissures at a stable rate of approximately 41.9 m<sup>3</sup>/hour, 56.9 m<sup>3</sup>/hour, and 75.0 m<sup>3</sup>/hour respectively. Subsequently, we compared numerically calculated stable water volumes with those estimated from field measurements for a working face advancement of 200m, 250m, and 300 m. The numerically calculated values were found to be approximately equal to measured average stable water volumes of about 40.0 m<sup>3</sup>/hour, 53.6 m<sup>3</sup>/hour, and 70.8 m<sup>3</sup>/hour, respectively. The minimal discrepancy between these two estimation methods indicates that our numerical calculation model accurately predicts surface water infiltration volume during coal seam mining under gully conditions.

(3) Based on a numerical calculation of the surface water infiltration of the coal seam under the gully mining, we put forward corresponding prevention and control measures such as surface fissures backfilling, construction of impervious artificial riverbed or impermeable membrane in the gully, construction of water conservation forest, and reasonable arrangement of mining time. Through the above-mentioned prevention and control measures, the surface water can be effectively blocked from entering the goaf, which minimizes the occurrence of mine water disasters and ensures safe mining.

### Acknowledgments

This research was financially supported by the National Natural Science Foundation of China (Grant No. 52204262, 52374255), Shaanxi Province Innovation Capability Support Program Project (Grant No. 2024RS-CXTD-44). The authors would like to thank the editors and anonymous reviewers for their comments and suggestions, which greatly helped us to improve this manuscript.

### Conflict of Interest

The authors declare no competing interests.

### References

- LIU S.L., LI W.P., WANG Q.Q. Height of the water-flowing fractured zone of the Jurassic coal seam in northwestern China. *Mine Water and the Environment*, **37** (2), 312, **2018**.
- GUI H.R., LIN M.L. Types of water hazards in China coalmines and regional characteristics. *Natural Hazards*, **84** (2), 1501, **2016**.
- The Comprehensive Research Group for Energy Consulting and Research. Strategic research on clean, efficient, sustainable exploitation and utilization of coal in China. *Strat Study CAE*, **17** (9), 1, **2015**.
- WU Q., FAN Z.L., ZHANG Z.W., ZHOU W.F. Evaluation and zoning of groundwater hazards in Pingshuo No. 1 underground coal mine, Shanxi Province, China. *Hydrogeology Journal*, **22** (7), 1693, **2014**.
- WU Q., LIU Y.Z., ZHOU W.F., LI B.Y., ZHAO B., LIU S.Q., SUN W.J., ZENG Y.F. Evaluation of water inrush vulnerability from aquifers overlying coal seams in the Menkeqing coal mine, China. *Mine Water and the Environment*, **34** (3), 258, **2014**.
- ZHU G., WU X., YU S., QIAN C., DONG Y.Y., ZHANG C.J., WU C. Surface Water Control for Mining Thick, Relatively Shallow Coal Seams in the Loess Area of Western China. *Mine Water and the Environment*, **37** (3), 442, **2018**.
- YIN H.Y., WEI J.C., LEFTICARIU L., GUO J.B., XIE D.L., LI Z.L., ZHAO P. Numerical simulation of water flow from the coal seam floor in a deep longwall mine in China. *Mine Water and the Environment*, **35** (2), 243, **2016**.
- ZHANG R., JIANG Z.Q., ZHOU H.Y., YANG C.W., XIAO S.J. Groundwater outbursts from faults above a confined aquifer in the coal mining. *Natural Hazards*, **71** (3), 1861, **2014**.
- DONG S.N., HU W.Y. Basic characteristics and main controlling factors of coal mine water hazard in China. *Coal Geology and Exploration*, **35**, 34, **2007**.
- SUN W.J., ZHOU W.F., JIAO J. Hydrogeological classification and water inrush accidents in China's coal mines. *Mine Water and the Environment*, **35** (2), 214, **2015**.
- WU Q., CUI F.P., ZHAO S.Q., LIU S.Q., ZENG Y.F., GU Y.W. Type classification and main characteristics of mine water disasters. *Journal of China Coal Society*, **38**, 561, **2013**.
- ZHU T.E., LI W.P., WANG Q.Q., HU Y.B., FAN K.F., DU J.F. Study on the height of the mining-induced water-conducting fracture zone under the Q2l loess cover of the Jurassic coal seam in Northern Shaanxi, China. *Mine Water and the Environment*, **39**, 57, **2020**.
- MU W.P., WU X., DENG R.C., HAO Q., QIAN C. Mechanism of water inrush through fault zones using a coupled fluid-solid numerical model: A case study in the Beiyangzhuang coal mine, Northern China. *Mine Water and the Environment*, **39**, 380, **2020**.
- LI H.L., BAI H.B. Simulation research on the mechanism of water inrush from fractured floor under the dynamic load induced by roof caving: taking the Xinji second coal mine as an example. *Arabian Journal of Geosciences*, **12** (15), 466, **2019**.

15. ZHANG S.C., GUO W.J., LI Y.Y., SUN W.B., YIN D.W. Experimental simulation of fault water inrush channel evolution in a coal mine floor. *Mine Water and the Environment*, **36** (3), 443, **2017**.
16. ZHOU Q.L., HERRERA J., HIDALGO A. The numerical analysis of fault-induced mine water inrush using the extended finite element method and fracture mechanics. *Mine Water and the Environment*, **37** (1), 185, **2018**.
17. LIU X.S., TAN Y.L., NING J.G., TIAN C.L., WANG J. The height of water-conducting fractured zones in longwall mining of shallow coal seams. *Geotechnical and Geological Engineering*, **33** (3), 693, **2015**.
18. QIU M., HUANG F.J., WANG Y., GUAN T., SHI L.Q., HAN J. Prediction model of water yield property based on GRA, FAHP and TOPSIS methods for Ordovician top aquifer in the Xinwen coalfield of China. *Environmental Earth Sciences*, **79** (22), 214, **2020**.
19. FAN K.F., LI W.P., WANG Q.Q., LIU S.L., XUE S., XIE C.Y., WANG Z.K. Formation mechanism and prediction method of water inrush from separated layers within coal seam mining: A case study in the Shilawusu mining area, China. *Engineering Failure Analysis*, **103**, 158, **2019**.
20. SHI L.Q., QIU M., WANG Y., QU X.Y., LIU T.H. Evaluation of water inrush from underlying aquifers using a modified water-inrush coefficient model and water-inrush index model: a case study in Feicheng coalfield, China. *Hydrogeology Journal*, **27**, 2105, **2019**.
21. LI L.P., ZHOU Z.Q., LI S.C., XUE Y.G., XU Z.H., SHI S.S. An attribute synthetic evaluation system for risk assessment of floor water inrush in coal mines. *Mine Water and the Environment*, **34** (3), 288, **2014**.
22. LI H.J., LI J.H., LI L., XU H., WEI J.J. Prevention of water and sand inrush during mining of extremely thick coal seams under unconsolidated Cenozoic alluvium. *Bulletin of Engineering Geology and the Environment*, **79**, 3271, **2020**.
23. DONG S.N., ZHENG L.W., TANG S.L., SHI P.Z. A scientometric analysis of trends in coal mine water inrush prevention and control for the period 2000-2019. *Mine Water and the Environment*, **39** (1), 3, **2020**.
24. LI H.J., CHEN Q.T., SHU Z.Y., LI L., ZHANG Y.C. On prevention and mechanism of bed separation water inrush for thick coal seams, a case study in China. *Environmental Earth Sciences*, **77** (22), 759, **2018**.
25. GUO W.B., BAI E.H., ZHAO G.B. Current status and progress on overburden and surface damage and prevention technology of high-intensity mining. *Journal of China Coal Society*, **45** (2), 509, **2020**.
26. YANG D.M., GUO W.B., TAN Y., WANG Y.X., MA X.C., LI Z. Lithology and fissure characteristics of overburden in high-intensity mining. *Journal of China Coal Society*, **44** (3), 786, **2019**.
27. LIU Y., LIU Q.M., LI W.P., LI T., HE J.H. Height of water-conducting fractured zone in coal mining in the soil-rock composite structure overburdens. *Environmental Earth Sciences*, **78** (7), 242, **2019**.
28. QIAN M.G., XU J.L. Behaviors of strata movement in coal mining. *Journal of China Coal Society*, **44** (4), 973, **2019**.
29. LI J.W., LIU C.Y., WANG W.C., WANG C.Y. Linkage-induced mechanism and control technology of pressure bump and surface geological damage in shallow coal seam mining of gully area. *Arabian Journal of Geosciences*, **12** (11), 349, **2019**.
30. YAN W.T., DAI H.Y., CHEN J.J. Surface crack and sand inrush disaster induced by high-strength mining: example from the Shendong coal field, China. *Geosciences Journal*, **22** (2), 347, **2018**.
31. SUI W.H., HANG Y., MA L., WU Z., ZHOU Y., LONG G. Interactions of overburden failure zones due to multiple-seam mining using longwall caving. *Bulletin of Engineering Geology and the Environment*, **74** (3), 1019, **2015**.
32. SUN W.J., WU Q., DONG D.L., JIAO J. Avoiding coal-water conflicts during the development of China's large coal-producing regions. *Mine Water and the Environment*, **31** (1), 74, **2012**.
33. WU Q., WANG M.Y. Characterization of water bursting and discharge into underground mines with multilayered groundwater flow systems in the North China coal basin. *Hydrogeology Journal*, **14** (6), 882, **2006**.
34. FAN L.M. On northwest China large coal bases groundwater monitoring engineering issues. *Coal Geology of China*, **30** (6), 87, **2018**.
35. FAN L.M., XIANG M.X., PENG J., MA X.D. Evolution analysis on springs in contiguous area of Maowusu desert and loess plateau. *Journal of China Coal Society*, **43** (1), 207, **2018**.
36. HUANG Q.X. Research on roof control of water conservation mining in shallow seam. *Journal of China Coal Society*, **42** (1), 50, **2017**.
37. CAO J., LI W.P. Numerical simulation of gas migration into mining-induced fracture network in the goaf. *International Journal of Mining Science and Technology*, **27**, 681, **2017**.
38. ZHAO Y.X., ZHANG K.N., SUN B., LING C.W., GUO J.H. Heat transfer and temperature evolution in underground mining-induced overburden fracture and ground fissures: Optimal time window of UAV infrared monitoring. *International Journal of Mining Science and Technology*, **34**, 31, **2024**.
39. ZHANG G.C., TAO G.Z., MENG X.J., LI Y., QU Z., XU R.H., YU S.C., CHEN S., ZHOU G.L., LUAN H.J. Failure law of weak overburden stratum underlying extra-thick alluvium. *Journal of China Coal Society*, **47**, 3998, **2022**.
40. HUANG B.X., LIU C.Y., XU J.L. Research on through degree of overlying strata fracture fissure induced by mining. *Journal of China University of Mining & Technology*, **39** (1), 45, **2010**.
41. LIU W.T., PANG L.F., XU B.C. Study on overburden failure characteristics in deep thick loose seam and thick coal seam mining. *Geomatics, Natural Hazards and Risk*, **11** (1), 632, **2020**.
42. JIA H.S., MA N.J., ZHAO X.D. "Open-close" law of longitudinal transfixion cracks in shallow buried coal face with thin bedrock. *Journal of China Coal Society*, **40** (12), 2787, **2015**.
43. WEI J.B., WANG S.M., SONG S.J., SUN Q. Numerical simulation on evolution law of overburden fractures and surface cracks in crossing ditch mining of shallow coal seam. *Coal Geology & Exploration*, **50** (10), 67, **2022**.
44. WU Y., HUANG Z., LI X.Z., JIANG C.L. Deformation and failure characteristics of overburden under thin bedrock and thick alluvium: A case study in Baodian coal mine. *Geotechnical and Geological Engineering*, **38**, 5213, **2020**.
45. TIAN C.L., LIU Y.B., YANG X.L., HU Q.T., WANG B. Development characteristics and field detection of overburden fracture zone in multiseam mining: A case study. *Energy Science & Engineering*, **8** (3), 602, **2019**.
46. ZHANG G.B., ZHANG W.Q., WANG C.H. Mining thick coal seams under thin bedrock-deformation and failure of overlying strata and alluvium. *Geotechnical and Geological Engineering*, **34** (5), 1553, **2016**.
47. ZHANG D.Y., SUI W.H., LIU J.W. Overburden failure associated with mining coal seams in close proximity in ascending and descending sequences under a large water body. *Mine Water and the Environment*, **37**, 322, **2017**.